Integrated nano-structured silicon waveguides and devices for high-speed optical communications

(Invited Paper)

Alan E. Willner, Lin Zhang (张 林), Yang Yue (岳 洋), and Xiaoxia Wu (武晓霞)

Department of Electrical Engineering, University of Southern California, Los Angeles, CA 90089, USA
∗E-mail: willner@usc.edu, linzhang@usc.edu, yyue@usc.edu, and xiaoxia@usc.edu

With progress in fabrication technology, integrated photonics plays an increasingly important role in high-speed optical communications, from monolithic transmitters and receivers for advanced optical modulation formats to on-chip subsystems for optical signal processing. We review our recent work on the highly tailorable physical properties of silicon waveguides for communication and signal processing applications, using slot structures. Controllable chromatic dispersion, nonlinearity, and polarization properties of the waveguides are presented, and the enabled wideband wavelength conversion, optical tunable delay, and signal processing of polarization-multiplexing data channels are discussed.

1. Introduction

Optical fiber communication has fueled the information technology revolution in the past two decades[1], and high-speed transport of huge volume of data relies on global optical communication systems. Various kinds of optical fibers have been developed not only as a transmission medium of information but also as a platform supporting functional devices. Integrated photonics has been intensely investigated for communication applications in recent years, and it potentially allows for cost-effective production and relatively easy packaging[2] as compared to the fiber-based devices. More importantly, strong light confinement and smaller chip size could assist in realizing power-efficient photonic devices, which enables highly desirable "green" information technology. Integrated photonics also plays an increasingly important role in datacom systems, such as computer-to-computer, chip-to-chip and even intra-chip communications, and serves as an enabling technology platform to build space-, power-, and spectrally efficient optical interconnection networks that could be seamlessly integrated with complementary metal-oxide-semiconductor (CMOS) electronics[3].

Besides some basic operations such as optical signals' modulation, transmission, and detection, high-speed optical communications may need certain advanced photonic signal processing functions[4] to overcome the speed bottleneck caused by electronics and achieve wavelength- and data-format-transparent signaling and routing. These functions include, but are not limited to, signal regeneration, wavelength conversion, optical sampling and time-division-demultiplexing, tunable delay, and multicasting and optical logics[5,6]. Many of them are based on nonlinear wave propagation effects assisted by tailorable chromatic dispersion and polarization properties. The ability of widely tailoring dispersion, nonlinearity, and polarization in integrated waveguides could thus be extremely important.

High index-contrast silicon waveguides have been considered as a building block of on-chip nonlinear signal processing devices. Nonlinear Kerr, Raman, and carrier effects[7−10], and dispersion manipulation[11−14] in the silicon strip and rib waveguides have been demonstrated. However, there are some design trade-offs that limit us to further improve the physical properties of the waveguides. For example, the high index contrast between the silicon core and waveguide cladding produces a tight confinement of light and thus high nonlinearity, but it tends to introduce strong and fast-changing waveguide dispersion that is dominant over material dispersion. It is difficult to obtain a wideband and flat dispersion profile when high nonlinearity is kept, and this trade-off may cause low nonlinear efficiency or limited operation bandwidth for communication applications.

One kind of nano-structured integrated waveguide, called slot waveguide, has recently been proposed[15], in which two high-index parts are laterally placed or vertically stacked, with a slot of tens of nanometers between them. The slot has low index of refraction, and the electric field in it is enhanced by the index contrast when polarized normal to the interfaces of high-index and low-index materials. By properly modifying structural parameters, one can confine a large fraction of light in the nano-scale slot layer to greatly control effective nonlinearity that depends on the slot material[16−19].
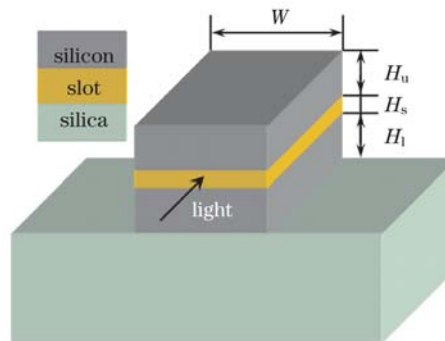

Fig. 1. Slot waveguide with silicon layers surrounding a highly nonlinear slot layer.

Moreover, the slot waveguides are multilayer structures and provide additional design freedom as compared to strip waveguides, thus exhibiting enhanced birefringence[20,21], tailorable dispersion[22−25], and improved modulation efficiency[26].

In this paper, we present some our recent work on tailoring physical properties of integrated waveguides using the slot structures, with an emphasis on their applications in high-speed optical communication systems. Chromatic dispersion, nonlinearity, and birefringence are examined and optimized over a wide wavelength band to design integrated wavelength converters, optical delay lines, and polarization-diverse devices (polarization splitters and rotators) that can deal with multi-channel operations of optical signals at more than 100-Gb/s bit rates.

2. Physical parameters and signal transmission

Figure 1 shows a slot waveguide, and the horizontal slot is surrounded by two silicon layers with air cladding. The waveguide substrate is 2-μm buried oxide. For high nonlinearity, we consider Si nano-crystal as the slot material. For the quasi-TM mode (vertically polarized), the discontinuity of its electric field causes a great enhancement of the local evanescent field near the interfaces of the slot and the silicon layers. When the slot layer is thin and the evanescent fields of the two silicon parts constructively interfere with each other, a large fraction of the guided mode is confined in the slot layer[15].

To characterize chromatic dispersion in the slot waveguides, we calculate the effective index of the quasi-TM mode as a function of wavelength using a finite-element mode solver (COMSOL Multiphysics 3.4), with the element size of 5, 40, and 100 nm for slot, silicon, and other regions, respectively. Material dispersion is taken into account for the Si nano-crystal slot[27], silicon[28], and silica substrate. Group velocity dispersion, $D = -(c/\lambda)\cdot(\mathrm{d}^2 n/\mathrm{d}\lambda^2)$, is calculated, where n is the effective index of refraction, and c and λ are the speed and wavelength of light in vacuum, respectively.

To calculate nonlinear coefficient γ, we use the Kerr nonlinear index of refraction n_2 and two-photon absorption (TPA) coefficient β_{TPA}, which correspond to the real and imaginary parts of γ respectively, varying with wavelength[29,30]. For silicon, when we calculate γ as a function of wavelength, the measurements given in Refs. [29,30] are fitted using six-order polynomials and averaged to consider the wavelength-dependent nonlinearity. For Si nano-crystal with 8% silicon excess, annealed at 800 °C, we choose $n_2 = 4.8\times10^{-17}$ m^2/W and $\beta_{\mathrm{TPA}} = 7\times10^{-11}$ m/W at 1550 nm[31]. For silica, $n_2 = 2.6\times10^{-20}$ m^2/W is used, and β_{TPA} is neglected. The nonlinear coefficient γ is computed with a transverse space resolution of 1 nm by using a full-vector model[32], in which the contributions of different materials to nonlinearity are weighted by optical mode distribution, and the longitudinal electric field of the mode is also considered. A figure of merit (FOM) is defined as the real part of γ divided by the imaginary part of γ times 4π, i.e., $\gamma_{\mathrm{re}}/(4\pi\gamma_{\mathrm{im}})$, to evaluate TPA effect. In a scalar model with a single nonlinear material, $\gamma_{\mathrm{re}} = 2\pi n_2/(\lambda A_{\mathrm{eff}})$ and

$\gamma_{\mathrm{im}} = \beta_{\mathrm{TPA}}/(2A_{\mathrm{eff}})$, where A_{eff} is the effective mode area. This FOM is equivalent to the commonly used FOM $n_2/(\lambda\beta_{\mathrm{TPA}})$[33].

High-speed signal propagation is simulated using carrier dynamic equation and nonlinear Schrödinger equation[7,11]. It is important to mention that we use a single Schrödinger equation to simulate all nonlinear Kerr effects, including self-phase modulation, cross-phase modulation, and cascaded four wave mixing interactions, by treating all these effects as an intra-channel effect. This is a comprehensive approach to dealing with the nonlinear interplay of all the optical frequency components contained in multiple data channels. Pseudo-random bit sequence (PRBS) with 8191 (i.e., $2^{13}-1$) bits is used in the simulations of evaluating signal quality factor (Q) and bit error rate.

The polarization splitters and rotators presented in this paper are essentially waveguide couplers. To characterize their performances, the finite-element mode solver is used to obtain the electric field ($\boldsymbol{E}$) distribution and propagation constant (β) of each supermode in the "couplers". In our designed polarization devices, E_z is less than 10^{-3} of E_x and E_y. This means that it is accurate enough to only consider the x- and y-components of $\boldsymbol{E}$. After substituting them into the following equation, we further verify the propagation characteristics of the polarization devices:

$$\boldsymbol{E}(x,y) = \sum_i k_i \boldsymbol{E}_i(x,y)\mathrm{e}^{\mathrm{j}\beta_i z}, \qquad (1)$$

where the vector fields in terms of the components can be expressed as

$$\begin{aligned} \boldsymbol{E}(x,y) &= E_x(x,y)\hat{\mathrm{x}} + E_y(x,y)\hat{y}, \\ \boldsymbol{E}_i(x,y) &= E_{ix}(x,y)\hat{\mathrm{x}} + E_{iy}(x,y)\hat{y}, \end{aligned} \qquad (2)$$

and k_i is the normalized coefficient for the linear superposition of the supermodes to generate an electric field input only in the input waveguide. Here $i = 1, 2$ for the two supermodes in the polarization splitter and $i = 1, 2, 3$ for the three supermodes in the polarization rotator.

3. Dispersion-tailored silicon waveguides for communication applications

Dispersion manipulation is extremely important for many of high-speed communication applications. For example, in signal transmission, the dispersion-induced data distortion dramatically increases as bit rate increases. Moreover, the highly tailorable dispersion could be useful for achieving optical signal processing functions. Low dispersion is essential to obtaining efficient nonlinear parametric interaction for wavelength conversion and optical sampling, while high dispersion is needed to produce tunable optical delay and pulse compression. In this section, we will discuss recently developed dispersion tailoring techniques using integrated waveguides.

3.1 Low dispersion over a wide wavelength band

Low dispersion and small relative group delay are

needed to reduce phase mismatch and pulse walk-off for strong nonlinear interaction of high-speed signals. Since short optical pulses in the high-speed signals occupy a wide bandwidth, low dispersion should be made available over a wide band where multi-channel high-speed signals exist. Silicon slot waveguides could provide such a dispersion profile.

With silicon nano-crystal in the slot, one can obtain low and flat dispersion by choosing waveguide width W = 500 nm, upper and lower silicon heights $H_u = H_l$ =180 nm, and slot height H_s = 47 nm. Figure 2 shows the flat dispersion profile within 0 ± 160 ps/(nm·km) obtained over a 244-nm wavelength range, from 1539 to 1783 nm. Since the on-chip waveguides are typically a few centimeters long, the accumulated dispersion over this band is quite small. There are two zero-dispersion wavelengths (ZDWs) located at 1580 and 1751 nm, respectively. The peak dispersion of 156 ps/(nm·km) is found at 1670 nm. Figure 2 shows that the dispersion peak value is decreased from 210.1 to 50.8 ps/(nm·km) as H_s varies from 46 to 49 nm. This provides an effective way to shift the dispersion profile at a rate of 53 ps/(nm·km) per nm. We note that the Si nano-crystal slot waveguides have a large index contrast between the slot and silicon layers and a small slot height, and this causes strong field enhancement in the slot. Since the overall dispersion is dominated by waveguide dispersion, the dispersion is highly sensitive to the slot height. To confirm this argument, we modify the slot height by 10 nm for H_s = 40, 80, and 120 nm (W = 500 nm, $H_u = H_l$ =180 nm), and the computed dispersion value is accordingly changed by 698, 339, and 195 ps/(nm·km) at 1650-nm
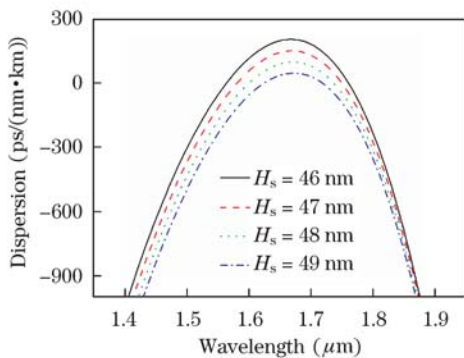

Fig. 2. For Si nano-crystal slot waveguides, dispersion profiles change with slot height.
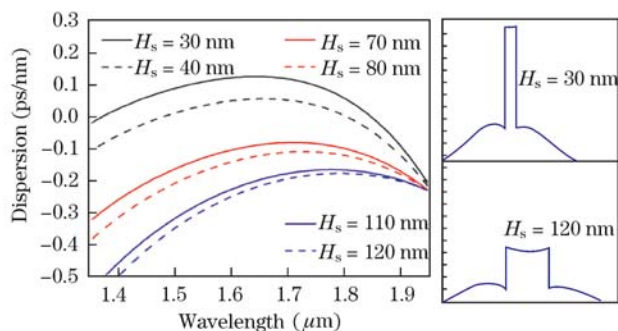

Fig. 3. For 10-cm Si nano-crystal slot waveguides, dispersion sensitivity changes with H_s.
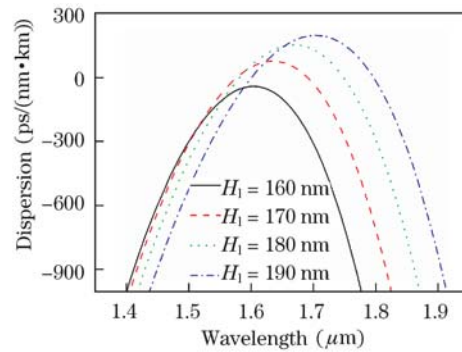

Fig. 4. Dispersion profile red-shifts as lower silicon height increases.

wavelength, as shown in Fig. 3. A small H_s induces strong field enhancement shown in Fig. 3, and the field enhancement causes an increased dispersion sensitivity to the slot height.

As shown in Fig. 4, the dispersion is changed by increasing the lower silicon height H_l. The dispersion curve is red-shifted as H_l increases. The right ZDW shifts by 106 nm, from 1696 to 1802 nm as H_l is changed from 170 to 190 nm. Generally, similar trends of dispersion tailoring are found for the Si nano-crystal slot waveguides as the upper silicon height and width are increased, so we do not show dispersion profile shift repeatedly.

With W = 500 nm, $H_u = H_l$ = 180 nm, H_s = 47 nm, the nonlinear coefficient γ and FOM are 2874 $(W \cdot m)^{-1}$ and 0.447, respectively, at 1550-nm wavelength. A small change in the slot height, from 46 to 49 nm, does not change γ and FOM much. Due to the strong field enhancement in the slot, the contribution of the Si nano-crystal slot to the overall FOM is dominant. This is confirmed by the fact that silicon's material FOM is 0.352 at 1550-nm wavelength, but the Si nano-crystal's material FOM $n_2/\lambda\beta_{\text{TPA}}$ is 0.4424, very close to the overall FOM. It is important to mention that the high nonlinear coefficient γ and low dispersion allow a great reduction of pump power for nonlinear optical signal processing on a chip.

Note that the slot mode is essentially the evanescent field of the optical wave guided in the silicon parts. Therefore, when shrinking the dimensional parameters of the silicon parts, one reduces the effective index of the slot mode and makes it closer to that of substrate modes. This causes mode coupling between them and thus a leakage of the guided mode to the substrate. The mode coupling also results in a sharp change of the effective index over wavelength, which produces negative dispersion at long wavelengths (around 2300 nm) where the coupling occurs. This explains why the silicon material dispersion is bent by waveguide dispersion so that the overall dispersion is relatively low and flat over a wide wavelength range. On the other hand, this determines that the overall dispersion has a convex profile and there are two ZDWs at most. Pursuing further flattened dispersion curves with even more ZDWs would require new dispersion tailoring techniques.

3.2 High dispersion over a wide wavelength band

Although high chromatic dispersion can suppress

nonlinear parametric processes, it could be quite use-ful for other signal processing applications such as pulse compression[34] and tunable optical delay[35,36]. High dispersion is often produced by resonance-related effects[37−39], in which both the real part and the imaginary part of the effective index of an optical wave change rapidly across the resonance wavelength. This determines the narrowband nature of high dispersion, and the dispersion bandwidth is just around tens of gigahertzs. Moreover, near the narrow dispersion band, high-speed signals could be distorted by higher-order dispersion. Generation of high dispersion over a wide wavelength band is thus desirable.

A slot waveguide structure with a strip waveguide integrated on the top is drawn in Fig. 5. They are vertically coupled. The effective index of the quasi-TM mode in the strip waveguide decreases with wavelength faster than that of the slot mode, and a strong mode coupling occurs around a certain wavelength where the effective indices are close to each other, as shown in Fig. 5. At the crossing-point, two supermodes (i.e., symmetric and anti-symmetric modes) are formed and experience a very sharp transition of mode shape from short to long wave-length in Fig. 5, which induces a high dispersion[40,41]. The strip waveguide, with a thickness of 255 nm and a width of 500 nm, is placed on the top of the slot waveg-uide, separated by a 500-nm-thick silica base layer. The low-index slot is a 40-nm silica layer, surrounded by two 160-nm silicon layers. At the crossing wavelength of 1.489 μm shown in Fig. 6, the symmetric mode has a dispersion of -181520 ps/(nm·km). It is obtained over a relatively small wavelength range of 3.5 nm for a 1% dispersion variation. Note that the waveguide disper-sion induced by the mode coupling is really dominant over material dispersion and the waveguide dispersion induced by the individual strip or the slot waveguide,
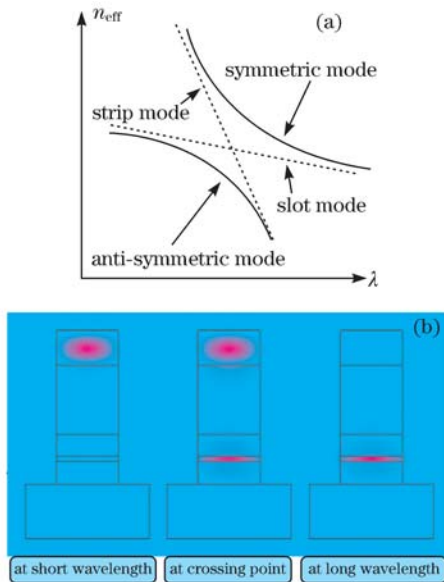

Fig. 6. Dispersion profiles of the symmetric and anti-symmetric modes, and a negative dispersion of -181520 ps/(nm·km) can be obtained from the symmetric mode.
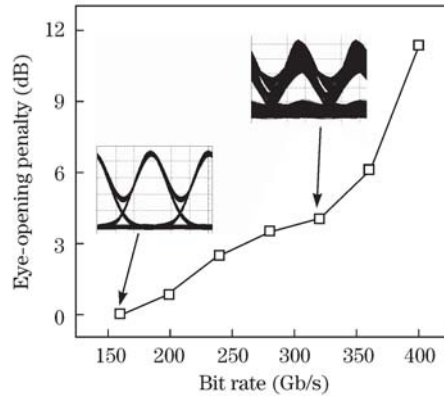
Fig. 7. Dispersion compensation for very high-speed signals transmitted over 11.4-km single mode fiber. Eye-opening penalty increases with bit rate. Eye-diagrams are in the same scale.

Fig. 8. Dispersion properties change with the waveguide width.

and thus the anti-symmetric mode has almost the same amount of positive dispersion.

Such a dispersion profile is wide enough to accom-modate high-speed signals for dispersion compensation. We simulate an optical return-to-zero (RZ) on-off-keying (OOK) signal transmitting over a 10.87-km-long single-mode fiber (SMF) link, where the chromatic dispersion is compensated using a 1-m-long waveguide with neg-ligible loss. Data rate is varied from 160 to 400 Gb/s.

Fig. 5. (a) Slot and strip modes strongly interact with each other due to index-matching at the crossing point, produc-ing a sharp index change of symmetric and anti-symmetric modes; (b) modal power distributions of the symmetric mode at different wavelengths.
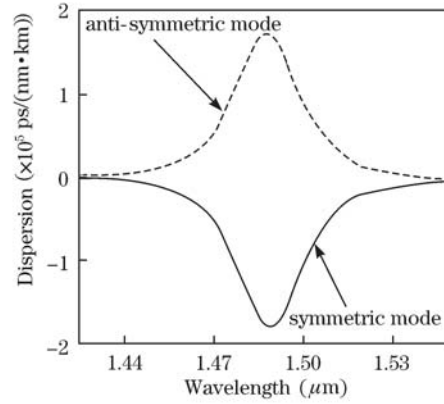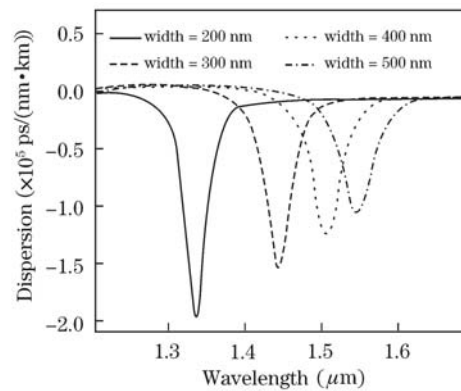
The waveguide width is 500 nm, and the strip waveguide thickness is 255 nm. The slot is 48 nm thick, surrounded by two 160-nm silicon layers. The silica base layer is 555 nm. A continuous-wave (CW) laser is tuned to the peak dispersion wavelength, where the SMF has a dispersion of 14.4 ps/(nm·km). Figure 7 shows that the dispersion is fully compensated for the 160-Gb/s signal with almost no penalty. However, as the bit rate increases, the signals start to be distorted by the third-order dispersion in the fibers, which are not compensated by the dispersion in the slot waveguide. An eye-opening penalty of 4 dB is induced when the signal bit rate is increased from 160 to 320 Gb/s.

We note that the dispersion profile can be shifted by varying structural parameters. Figure 8 shows that shrinking the waveguide width from 500 to 200 nm can shift the dispersion peak wavelength from 1336 to 1546 nm, with base thickness of 500 nm, strip thickness of 255 nm, slot thickness of 40 nm, and surrounding layers of 160 nm. Accordingly, the dispersion peak value becomes less negative, from -197297 to -105396 ps/(nm·km).

The dispersion bandwidth can be even broadened further for both telecom systems and optical signal processing, e.g., for achieving multi-channel dispersion compensation or a tunable optical delay line[35,36]. Dispersion can be flattened by cascading some waveguide sections with the modified structural parameter, each having a shifted dispersion profile. As an example, Fig. 9(a) shows that the strip waveguide has a slightly tailored waveguide width with the same vertical dimensions of the slot-waveguide and the silica
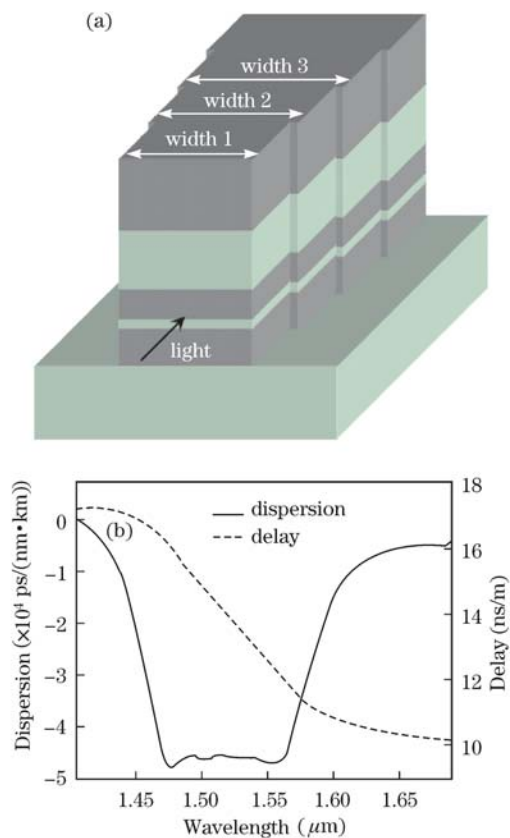

Fig. 9. (a) Waveguides with variable waveguide width are cascaded; (b) flat dispersion of -46100 ps/(nm·km) is obtained over 91 nm.

base, and the dispersion curve shifts over wavelength, as shown in Fig. 8. The length of each waveguide section is determined according to the dispersion peak values of the shifted dispersion profiles. A flat dispersion of -46100 ps/(nm·km) can be achieved from 1473 to 1564 nm, with a bandwidth of 91 nm, when the width varies from 565 to 500, 445, 390, and 340 nm. The length ratios are 26%, 17%, 17%, 7%, and 33%, respectively, with a variance of 623 ps/(nm·km), less than 1.4% of the mean dispersion.

Note that varying the waveguide width would be more fabrication friendly than changing other structural parameters and a smooth change of the width can be easily realized by e-beam lithography. A tunable optical delay of 4.2 ns/m based on conversion/dispersion approach[35,36] can be obtained using such on-chip waveguides, which is able to buffer 420 bits of signals at 100 Gb/s using a 1-m-long waveguide. It is important to mention that the flattened strong dispersion with small ripples is necessary to keep good signal quality of high-speed signals after wavelength conversion and dispersion-induced group delay by limiting data distortion caused by the third-order dispersion[42].

4. Polarization-controlled devices for polarization multiplexing system

In the past two decades, wavelength-division multiplexing (WDM) and time-division multiplexing (TDM) have been employed to greatly increase the capacity of fiber-optic communication systems[43]. Recently, advanced modulation formats, including multilevel phase-shift-keying and polarization-multiplexing (Pol-Mux) schemes[44,45], have been widely recognized as an effective method to achieve higher spectral efficiency. Moreover, these techniques require relatively low-speed electronics to enable high-speed communications in terms of bits/s. They might also be more cost-effective and power-efficient.

Pol-Mux, one of the commonly used advanced modulation formats, provides a straightforward method to double the spectral efficiency in terms of bits/(s·Hz)[45]. However, the polarization of an optical wave is at the heart of different data degrading effects, such as polarization-dependent-loss[46]. Recent reports have shown that differential group delay (DGD) and polarization mode dispersion (PMD) can have a dramatic impact on the performance of the Pol-Mux system[47]. Therefore, the control of the signal's state-of-polarization is quite desirable.

On the other hand, in the on-chip scenario, because of the high index contrast in the integrated devices, one of the main issues is the serious polarization dependence of their performance. As an example, one can see, from Fig. 10, different dispersion profiles of the x- and y-polarized fundamental modes in the silicon nano-crystal slot waveguide ($W = 500$ nm, $H_u = H_l = 180$ nm, and $H_s = 47$ nm). Strong polarization dependence of chromatic dispersion is demonstrated. At 1550 nm, the slot mode (y-polarization) has a dispersion of -110.9 ps/(nm·km). For x-polarization, the dispersion changes to the
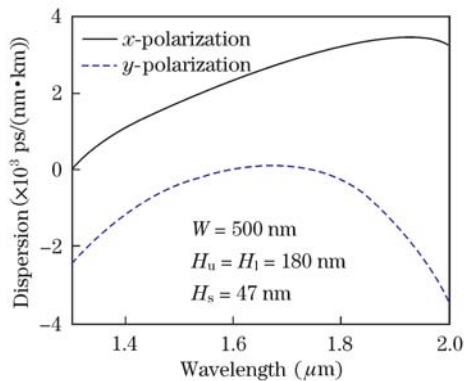
Fig. 10. Dispersion profiles of x- and y-polarized fundamental modes in slot waveguide.
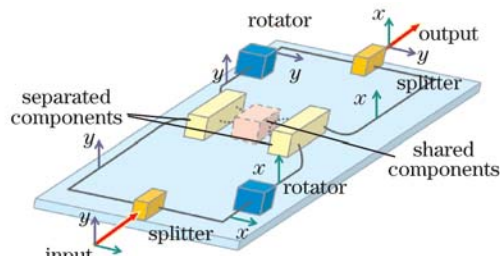

Fig. 11. On-chip polarization diversity scheme.

anomalous dispersion region with a value of 2100.9 ps/(nm·km). Theoretically, polarization-independent integrated devices can be achieved by accurately controlling the geometric parameters[48]. However, it is not trivial in real fabrication. A 5-nm fabrication variation might introduce a DGD up to 6 ps for a 5-cm-long waveguide[49]. For high-speed communications (more than 100 Gb/s), 6 ps is close to the time length of one bit.

To overcome this problem, a polarization diversity scheme as shown in Fig. 11 has been proposed[49,50]. The input light is separated according to the polarization state after passing through the first polarization splitter. Then, the polarization of the x-polarized light is rotated by 90° by the polarization rotator so that the two original polarization states of the light experience the same responses from the sequent signal-manipulating devices in the two arms as these devices are designed to be identical. Note that there might also be some shared components between the two arms as shown in Fig. 11. After the second 90° polarization rotator and polarization combiner, the input light with arbitrary polarization experiences polarization-insensitive operation. The polarization diversity approach can find an important application in coherent receivers[51]. Compared with conventional detection techniques, coherent detection can provide compensation for all linear impairments (e.g., dispersion, PMD) and better noise resilience[52] in high-speed signaling. Note that polarization splitters and rotators are the crucial devices in the polarization diversity system, and we discuss them in the following.

4.1 Polarization splitter

A polarization splitter is a device that can split the incident beam into two beams at the two orthogonal polarizations. Integrated polarization splitters have been realized using directional couplers[53], Mach-Zehnder interferometers[54], multimode interferences[55], mode evolution[56], and photonic crystals[57]. Also, based on a novel waveguide structure, the slot waveguide, researchers have proposed and demonstrated different polarization splitters[58,59]. In these slot-waveguide-based polarization splitters, the polarization dependence of waveguide coupling is designed to obtain an even integer ratio (i. e., 2) for the two polarization states' coupling lengths. This may cause a compromise to the device size or the operation bandwidth of the polarization splitter.

Using two horizontally-slotted waveguides, the polarization dependence of the strip waveguide coupler[60] can be pronouncedly enhanced. As in the horizontal slot waveguide coupler, a fair amount of the y-polarized mode is confined within the slots and experiences a relatively low index contrast between the air and silica slots. Consequently, the coupling of y-polarized mode is improved, which further enhances the polarization dependence. As a result, the ratio between the x- and y-polarized coupling lengths is increased remarkably. In this case, when the power of the y-polarized (quasi-TM) mode is completely transferred from the input waveguide to the other waveguide, almost all of the power of the x-polarized (quasi-TE) mode remains in the input waveguide. This means that only one coupling length of the strongly coupled polarization is needed to achieve polarization splitting, which allows for a further reduction of the splitter's size and a released requirement on the coupling length ratio.

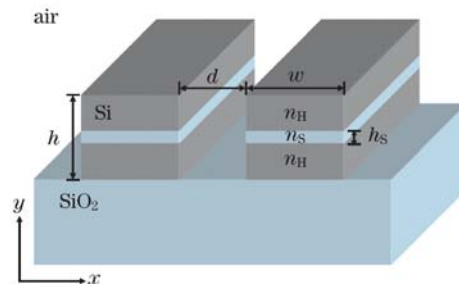Figure 12 shows the cross-section of the horizontally-

Fig. 12. Cross-section view of the horizontally-slotted waveguide polarization splitter.
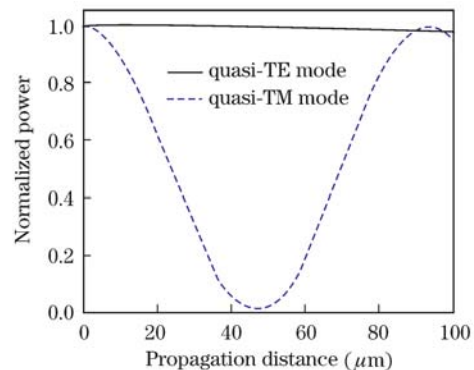

Fig. 13. Exchange of the normalized power along the propagation distance of the quasi-TE and quasi-TM modes at the input waveguide.
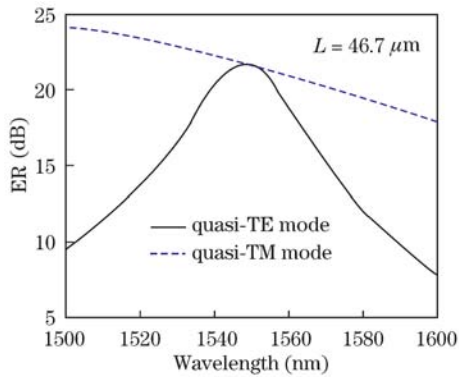
Fig. 14. ER of the quasi-TE and quasi-TM mode in a slot waveguide splitter at one coupling length.

slotted polarization splitter. The silicon polarization splitter has silica slots and a silica substrate. At 1550 nm, the refractive indices of silicon (n_H) and silica (n_S) are equal to 3.4764 and 1.4440, respectively. w, h, d, and h_S are the waveguide width, height, spacing and slot thickness, respectively. The optimized splitter parameters are $w = 500$ nm, $h = 360$ nm, $d = 500$ nm, and $h_S = 60$ nm.

Figure 13 shows that the normalized powers of the quasi-TE and quasi-TM modes in the input slot waveguide of the coupler as a function of the propagation distance. Owing to the large difference between L_{TE} and L_{TM}, most of the quasi-TE mode (99.35%) remains in the input waveguide while the quasi-TM mode is fully coupled to the output waveguide. Introducing horizontal slot remarkably enhances the polarization dependence of the coupling, and the ratio of the coupling lengths is increased up to 21.

The extinction ratios (ER) of the quasi-TE mode in the input waveguide and the quasi-TM mode in the output waveguide as a function of wavelength at $L = 46.7$ μm is shown in Fig. 14. ERs are around 22 dB for both polarization modes at 1550 nm. Furthermore, we examine the wavelength dependences of the ERs. For the quasi-TM mode in the output waveguide, its ER decreases monotonously with wavelength. Both L_{TE} and L_{TM} decrease with wavelength, and the ratio L_{TE}/L_{TM} decreases. For the input waveguide, the power of the quasi-TE mode changes negligibly, while the power of the quasi-TM mode increases tremendously. Consequently, the ER of the quasi-TE mode reduces when the wavelength is shifted away from 1550 nm. The splitter exhibits an 18-nm bandwidth for ER>20 dB.

4.2 Polarization rotator

A polarization rotator can rotate the incident beam from one polarization to another. The simple act of on-chip rotation of the polarization by 90° is not trivial. To realize polarization rotation, methods such as acousto-optic[61] or electro-optical[62] effects have been used. Passive polarization rotators have also been extensively studied to facilitate the fabrication and reduce the cost. Reported techniques that require precise fabrication of longitudinally varying structures include using photonic crystal patterns[63], periodic asymmetric waveguides[64], waveguide tapers[65], and an off-axis

double-core structure[66,67]. Slanted-sidewall waveguides are also used to realize polarization rotation[68]. A polarization rotator with a uniform and vertical sidewall structure over propagation direction is highly desired to reduce the fabrication complexity.

Enabled by wave coupling through an intermediate, multimode, uniform waveguide, 90° polarization rotation can be achieved efficiently. Figures 15(a) and (b) show the coupling efficiency of coupled waveguides with the 90° rotated mirror structure. The simulation results indicate that the electric fields of the refractive index matched waveguides, as illustrated in Fig. 15(a), cannot couple with each other, which is attributed to the fact that their electric fields are mostly orthogonal to one another. For the structure in Fig. 15(b), the modes of the two waveguides can couple mutually and generate two supermodes, which are analogous to a symmetric mode and an antisymmetric mode in regular directional couplers. Although the electric fields have parallel components within the coupling region, the coupling effect is very weak since the coupling length of these two waveguides is relatively long. We find that the coupling length of scheme (b) is around 1.2 mm for the same structural parameters as in scheme (c).

By introducing WG 2 near WGs 1 and 3, the coupling between WGs 1 and 3 is significantly enhanced
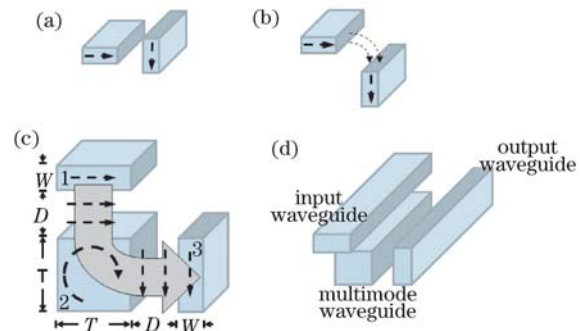

Fig. 15. Operating principle of (a) no coupling case, (b) weak coupling case, and (c) proposed 90° polarization rotator using wave coupling through an intermediate multimode waveguide; (d) schematic of proposed 90° polarization rotator.

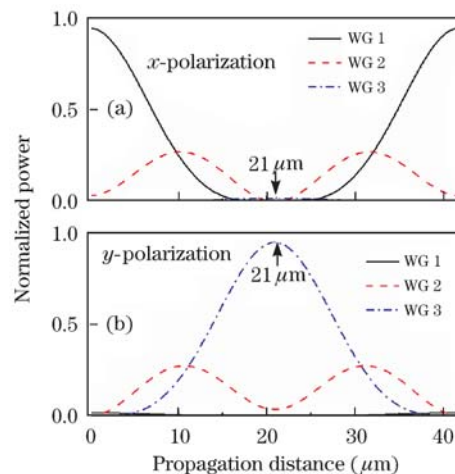
Fig. 16. (a) X-polarized and (b) y-polarized normalized power exchange along the propagation distance in three waveguides.
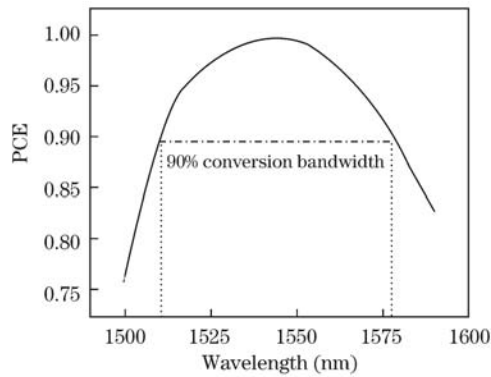
Fig. 17. PCE as a function of wavelength and >90% PCE bandwidth.

and the polarization rotator becomes more compact, as illustrated in Fig. 15(c). The electric field of the TE_{01} mode in WG 2 has a parallel electric field component to that of x-polarized fundamental mode in WG 1. Also, WG 2 has a parallel electric field component to that of the y-polarized fundamental mode in WG 3. Good electric field alignment produces a large coupling coefficient, which gives efficient energy transfer. As a result, the coupling length of scheme (c) is reduced to 21 μm, around 1/60 of the coupling length of scheme (b).

WGs 1, 2, and 3 are made of silicon and we choose silica as the cladding. To match the effective refractive index of the TE_{01} mode in multimode WG 2 with those of the x- and y-polarized fundamental modes in WGs 1 and 3, the parameters of W=182 nm, D=300 nm, and T=500 nm are chosen.

Figures 16(a) and (b) show the normalized power transfer of the x- and y-polarizations along the propagation distance. We note that the conversion length of the power from WGs 1 to 3 is around 21 μm, which is twice the conversion length of the TE_{01} mode in WG 2. From 0 to 10.5 μm, the energy is transferred from the x-polarized fundamental mode in WG 1 to the TE_{01} mode in WG 2. Meanwhile, the TE_{01} mode in WG 2 is coupled with the y-polarized fundamental mode in WG 3 and transfers the power to WG 3. In this process, the power in WG 1 decreases while the power accumulates in WGs 2 and 3. At the end of this process (10.5 μm), the power in WG 1 is equal to the power of WG 2 along the x-polarization, and the power of WG 2 along the y-polarization is equal to the power in WG 3. From 10.5 to 21 μm, the powers in WGs 1 and 2 decrease simultaneously and transfer to WG 3, resulting in the power in WG 3 reaching its maximum at 21 μm. The result illustrates that an ER of 17.22 dB can be achieved.

Polarization conversion efficiency (PCE) is a key parameter in evaluating the property of polarization rotators, which is defined as the percentage of the power transfer from the input polarized mode to the output orthogonally polarized mode. We further examine the PCE as a function of wavelength in order to evaluate the performance of the proposed polarization rotator. Figure 17 indicates that, for a PCE above 90%, the polarization rotator with the proposed parameters has a 68-nm bandwidth around 1543 nm.

5. Conclusion

We have shown that the physical properties of integrated silicon waveguides, such as dispersion, nonlinearity, and birefringence, could be highly controllable by using nano-structured slots. High and low dispersions are achieved over a large wavelength range, which is useful for nonlinear optical signal processing of high-speed signals. Strong birefringence can be obtained in various types of waveguide couplers, which can realize efficient polarization splitting and rotating in polarization-diverse operations of Pol-Muxed data channels.

References

1. I. P. Kaminow, T. Li, and A. E. Willner, *Optical Fiber Telecommunications* (5th edn.) (Elsevier, Amsterdam, 2008).
2. R. G. Hunsperger, *Integrated Optics: Theory and Technology* (Springer, Berlin, 2009).
3. R. G. Beausoleil, J. Ahn, N. Binkert, A. Davis, D. Fattal, M. Fiorentino, N. P. Jouppi, M. Mclaren, C. M. Santori, R. S. Schreiber, S. M. Spillane, D. Vantrease, and Q. Xu, in *Proceedings of Integrated Photonics and Nanphotonics Research and Applications* ITuD2 (2008).
4. H. Ishikawa, *Ultrafast All-Optical Signal Processing Devices* (John Wiley & Sons, Huboken, 2008).
5. J. Hansryd, P. A. Andrekson, M. Westlund, J. Li, and P.-O. Hedekvist, IEEE J. Sel. Top. Quantum Electron. **8,** 506 (2002).
6. K. Igarashi and K. Kikuchi, IEEE J. Sel. Top. Quantum Electron. **4,** 551 (2008).
7. Q. Lin, O. J. Painter, and G. P. Agrawal, Opt. Express **15,** 16604 (2007).
8. R. Dekker, N. Usechak, M. Förstm, and A. Driessen, J. Phys. D: Appl. Phys. **40,** R249 (2007).
9. H. K. Tsang and Y. Liu, Semiconduct. Sci. Technol. **23,** 064007 (2008).
10. R. M. Osgood, Jr., N. C. Panoiu, J. I. Dadap, X. Liu, X. Chen, I.-W. Hsieh, E. Dulkeith, W. M. Green, and Y. A. Vlasov, Adv. Opt. Photon. **1,** 162 (2009).
11. L. Yin, Q. Lin, and G. P. Agrawal, Opt. Lett. **31,** 1295 (2006).
12. E. Dulkeith, F. N. Xia, L. Schares, W. M. J. Green, and Y. A. Vlasov, Opt. Express **14,** 3853 (2006).
13. A. C. Turner, C. Manolatou, B. S. Schmidt, M. Lipson, M. A. Foster, J. E. Sharping, and A. L. Gaeta, Opt. Express **14,** 4357 (2006).
14. X. Liu, W. M. J. Green, X. Chen, I.-W. Hsieh, J. I. Dadap, Y. A. Vlasov, and R. M. Osgood, Jr., Opt. Lett. **33,** 2889 (2008).
15. V. R. Almeida, Q. F. Xu, C. A. Barrios, and M. Lipson, Opt. Lett. **29,** 1209 (2004).
16. P. Sanchis, J. Blasco, A. Martinez, and J. Marti, J. Lightwave Technol. **25,** 1298 (2007).
17. C. Koos, L. Jacome, C. Poulton, J. Leuthold, and W. Freude, Opt. Express **15,** 5976 (2007).
18. P. Muellner, M. Wellenzohn, and R. Hainberger, Opt. Express **17,** 9282 (2009).
19. Y. Yue, L. Zhang, J. Wang, Y. Xiao-Li, R. G. Beausoleil, and A. E. Willner, in *Proceedings of Lasers and Electro-*

Optics (CLEO) 2010 CThR6 (2010).

20. S. H. Yang, M. L. Cooper, P. R. Bandaru, and S. Mookherjea, Opt. Express **16,** 8306 (2008).

21. H. G. Yoo, Y. Fu, D. Riley, J. H. Shin, and P. M. Fauchet, Opt. Express **16,** 8623 (2008).

22. J. Jágerská, N. Le Thomas, R. Houdré, J. Bolten, C. Moormann, T. Wahlbrink, J. Ctyroký, M. Waldow, and M. Först, Opt. Lett. **32,** 2723 (2007).

23. A. Di Falco, L. O'Faolain, and T. F. Krauss, Appl. Phys. Lett. **92,** 083501 (2008).

24. R. Spano, J. V. Galan, P. Sanchis, A. Martinez, J. Martí, and L. Pavesi, in *Proceedings of Group IV Photonics* 314 (2008).

25. Z. Zheng, M. Iqbal, and J. Liu, Opt. Commun. **281,** 5151 (2008).

26. T. Baehr-Jones, M. Hochberg, G. Wang, R. Lawson, Y. Liao, P. A. Sullivan, L. Dalton, A. K. Y. Jen, and A. Scherer, Opt. Express **13,** 5216 (2005).

27. R. Spano, J. V. Galan, P. Sanchis, A. Martinez, J. Martí, and L. Pavesi, in *Proceedings of Group IV Photonics* 314 (2008).

28. E. D. Palik, *Handbook of Optical Constants of Solids* (Academic, San Diego, 1998).

29. A. D. Bristow, N. Rotenberg, and H. M. van Driel, Appl. Phys. Lett. **90,** 191104 (2007).

30. Q. Lin, J. Zhang, G. Piredda, R. W. Boyd, P. M. Fauchet, and G. P. Agrawal, Appl. Phys. Lett. **90,** 021111 (2007).

31. R. Spano, N. Daldosso, M. Cazzanelli, L. Ferraioli, L. Tartara, J. Yu, V. Degiorgio, E. Jordana, J. M. Fedeli, and L. Pavesi, Opt. Express **17,** 3941 (2009).

32. S. Afshar and T. M. Monro, Opt. Express **17,** 2298 (2009).

33. V. Mizrahi, K. W. Delong, G. I. Stegeman, M. A. Saifi, and M. J. Andrejco, Opt. Lett. **14,** 1140 (1989).

34. T. Inoue and S. Namiki, Laser Photon. Rev. **2,** 83 (2008).

35. Y. Wang, C. Yu, L.-S. Yan, A. E. Willner, R. Roussev, C. Langrock, and M. M. Fejer, in *Proceedings of ECOC (Europe Conference on Optical Communication) 2005* Th1.3.3 (2005).

36. J. E. Sharping, Y. Okawachi, J. van Howe, C. Xu, Y. Wang, A. E. Willner, and A. L. Gaeta, Opt. Express **13,** 7872 (2005).

37. C. K. Madsen, G. Lenz, A. J. Bruce, M. A. Capuzzo, L. T. Gomez, T. N. Nielsen, and I. Brener, Opt. Lett. **24,** 1555 (1999).

38. M. Hossein-Zadeh and K. J. Vahala, IEEE Photon. Technol. Lett. **19,** 1045 (2007).

39. L. Zhang, M. Song, J.-Y. Yang, R. G. Beausoleil, and A. E. Willner, in *Proceedings of Integrated Photonics and Nanophotonics Research and Applications (IPNRA) 2008* IWA3 (2008).

40. U. Peschel, T. Peschel, and F. Lederer, Appl. Phys. Lett. **67,** 2111 (1995).

41. H. Subbaraman, T. Ling, Y. Jiang, M. Y. Chen, P. Cao, and R. T. Chen, Appl. Opt. **46,** 3263 (2007).

42. S. R. Nuccio, O. F. Yilmaz, X. Wang, H. Huang, J. Wang, X. Wu, and A. E. Willner, "Higher-order dispersion compensation to enable a 3.6-μs wavelength- maintaining delay of a 100-Gb/s DQPSK signal" Opt. Lett. (to be published).

43. S. Kawanishi, H. Takara, K. Uchiyama, I. Shake, and K. Mori, Electron. Lett. **35,** 826 (1999).

44. P. J. Winzer and R. J. Essiambre, J. Lightwave Technol. **24,** 4711 (2006).

45. C. Wree, N. Hecker-Denschlag, E. Gottwald, P. Krummrich, J. Leibrich, E. D. Schmidt, B. Lankl, and W. Rosenkranz, IEEE Photon. Technol. Lett. **15,** 1303 (2003).

46. N. Y. Kim, D. Lee, H. Yoon, J. Park, and N. Park, IEEE Photon. Technol. Lett. **14,** 104 (2002).

47. D. van den Borne, N. E. Hecker-Denschlag, G. D. Khoe, and H. de Waardt, J. Lightwave Technol. **23,** 4004 (2005).

48. T. Fujisawa and M. Koshiba, Opt. Lett. **31,** 56 (2006).

49. H. Fukuda, K. Yamada, T. Tsuchizawa, T. Watanabe, H. Shinojima, and S. I. Itabashi, Opt. Express **16,** 4872 (2008).

50. T. Barwicz, M. R. Watts, M. A. Popovic, P. T. Rakich, L. Socci, F. X. Kartner, E. P. Ippen, and H. I. Smith, Nature Photon. **1,** 57 (2007).

51. C. R. Doerr, P. J. Winzer, Y. K. Chen, S. Chandrasekhar, M. S. Rasras, L. Chen, T. Y. Liow, K. W. Ang, and G. Q. Lo, J. Lightwave Technol. **28,** 520 (2010).

52. E. Ip, A. P. T. Lau, D. J. F. Barros, and J. M. Kahn, Opt. Express **16,** 753 (2008).

53. I. Kiyat, A. Aydinli, and N. Dagli, IEEE Photon. Technol. Lett. **17,** 100 (2005).

54. T. K. Liang and H. K. Tsang, IEEE Photon. Technol. Lett. **17,** 393 (2005).

55. J. M. Hong, H. H. Ryu, S. R. Park, J. W. Jeong, S. G. Lee, E. H. Lee, S. G. Park, D. Woo, S. Kim, and B. H. O, IEEE Photon. Technol. Lett. **15,** 72 (2003).

56. M. R. Watts, H. A. Haus, and E. P. Ippen, Opt. Lett. **30,** 967 (2005).

57. E. Schonbrun, Q. Wu, W. Park, T. Yamashita, and C. J. Summers, Opt. Lett. **31,** 3104 (2006).

58. J. B. Xiao, X. Liu, and X. H. Sun, Jpn. J. Appl. Phys. **47,** 3748 (2008).

59. Y. Ma and D. Huang, in *Proceedings of Group IV Photonics (GFP)* 297 (2008).

60. H. Fukuda, K. Yamada, T. Tsuchizawa, T. Watanabe, H. Shinojima, and S. Itabashi, Opt. Express **14,** 12401 (2006).

61. Y. Ohmachi and J. Noda, IEEE J. Quantum Electron. **13,** 43 (1977).

62. R. C. Alferness and L. L. Buhl, Appl. Phys. Lett. **38,** 655 (1981).

63. A. D. Bristow, V. N. Astratov, R. Shimada, I. S. Culshaw, M. S. Skolnick, D. M. Whittaker, A. Tahraoui, and T. F. Krauss, IEEE J. Quantum Electron. **38,** 880 (2002).

64. T. Mangeat, L. Escoubas, F. Flory, L. Roussel, M. De Micheli, and P. Coudray, Opt. Express **15,** 12436 (2007).

65. N. Feng, R. Sun, J. Michel, and L. C. Kimerling, Opt. Lett. **32,** 2131 (2007).

66. H. Fukuda, K. Yamada, T. Tsuchizawa, T. Watanabe, H. Shinojima, and S. Itabashi, Opt. Express **16,** 2628 (2008).

67. Z. Wang and D. Dai, J. Opt. Soc. Am. B **25,** 747 (2008).

68. H. Deng, D. O. Yevick, C. Brooks, and P. E. Jessop, J. Lightwave Technol. **23,** 432 (2005).